

# Demonstration of Muon-Beam Transverse Phase-Space Compression

A. Antognini,<sup>1,2,\*</sup> N. J. Ayres,<sup>1</sup> I. Belosevic,<sup>1,†</sup> V. Bondar,<sup>1</sup> A. Eggenberger,<sup>1</sup> M. Hildebrandt,<sup>2</sup>  
R. Iwai,<sup>1</sup> D. M. Kaplan,<sup>3</sup> K. S. Khaw,<sup>1,‡</sup> K. Kirch,<sup>1,2</sup> A. Knecht,<sup>2</sup> A. Papa,<sup>2,4</sup> C. Petitjean,<sup>2</sup>  
T. J. Phillips,<sup>3</sup> F. M. Piegsa,<sup>1,§</sup> N. Ritjoho,<sup>2</sup> A. Stoykov,<sup>2</sup> D. Taqqu,<sup>1</sup> and G. Wichmann<sup>1,¶</sup>

(muCool collaboration)

<sup>1</sup>*Institute for Particle Physics and Astrophysics, ETH Zürich, 8093 Zürich, Switzerland*

<sup>2</sup>*Paul Scherrer Institute, 5232 Villigen-PSI, Switzerland*

<sup>3</sup>*Illinois Institute of Technology, Chicago, IL 60616 USA*

<sup>4</sup>*Dipartimento di Fisica, Università di Pisa, and INFN sez. Pisa, Largo B. Pontecorvo 3, 56127 Pisa, Italy*

(Dated: April 21, 2022)

We demonstrate the efficient transverse compression of a 12.5 MeV/c muon beam stopped in a helium gas target featuring a vertical density gradient and strong crossed electric and magnetic fields. The vertical spread of the muon stopping distribution was reduced from 10 to 0.7 mm within 3.5  $\mu$ s. The simulation including proper cross sections for low-energy  $\mu^+$ -He elastic collisions and the charge exchange reaction  $\mu^+ + \text{He} \longleftrightarrow \text{Mu} + \text{He}^+$  describes the measurements well. By combining the transverse compression stage with a previously demonstrated longitudinal compression stage, we can improve the phase space density of a  $\mu^+$  beam by a factor of  $10^{10}$  with  $10^{-3}$  efficiency.

Next generation precision experiments with muons and muonium atoms [1], such as muon  $g - 2$  and EDM measurements [2–4], muonium spectroscopy [5], and muonium gravity measurements [6, 7], require high-intensity muon beams at low energy with small transverse size and energy spread. The standard surface muon beams currently available do not fulfill these requirements. To improve the quality of the muon beam, phase space cooling techniques are needed. However, conventional methods, such as stochastic cooling [8] and electron cooling [9], are not applicable due to the short muon lifetime of 2.2  $\mu$ s. Alternative beam cooling techniques based on muon energy moderation in materials have been developed [10, 11], however, they typically suffer from low cooling efficiencies ( $< 10^{-4}$ ).

At the Paul Scherrer Institute, we are developing a novel device (muCool) that produces a high-quality muon beam, reducing the full (transverse and longitudinal) phase space of a standard  $\mu^+$  beam by 10 orders of magnitude with  $10^{-3}$  efficiency [12]. The whole device is placed inside a 5 T magnetic field, pointing in the  $+z$ -direction, as sketched in Fig. 1. First, a surface muon beam propagating in the  $-z$ -direction is stopped in a few mbar of helium gas at cryogenic temperature, reducing the muon energy to the eV range. The stopped muons are then guided into a sub-mm spot using a combination of strong electric and magnetic fields and gas density gradients in three stages.

In the first stage (transverse compression), the electric field is perpendicular to the applied magnetic field and at  $45^\circ$  with respect to the  $x$ -axis:  $\vec{E} = (E_x, E_y, 0)$ , with  $E_x = E_y \approx 1$  kV/cm. In vacuum, applying such crossed electric and magnetic fields would prompt the stopped muons to drift in the  $\hat{E} \times \hat{B}$ -direction, performing cycloidal motion with frequency  $\omega = eB/m_\mu$  (cyclotron frequency), where  $m_\mu$  is the muon mass.

However, in the muCool device, the muons also collide with He gas atoms with an average frequency  $\nu_c$ , which depends on the gas density, elastic  $\mu^+$ -He cross section, and  $\mu^+$ -He relative velocity. These collisions lead to muon energy loss and change of direction. Thus, the muon motion is modified compared to that in vacuum, so that the muon drift velocity also acquires a component in the  $\hat{E}$ -direction, making muons drift at an angle  $\theta$  relative to the  $\hat{E} \times \hat{B}$ -direction. The average drift angle  $\theta$  is proportional to the collision frequency  $\nu_c$  [13]:

$$\tan \theta = \frac{\nu_c}{\omega}. \quad (1)$$

The reason for such behavior is as follows: for  $\nu_c > \omega$ , the muon will not complete the full period of the cycloidal motion before the next collision (blue trajectory in Fig. 1), resulting in a large drift angle  $\theta$ . If  $\nu_c < \omega$ , the muon will perform several periods of cycloidal motion between collisions, resulting in a smaller drift angle  $\theta$  (green trajectory in Fig. 1).

We use this feature to manipulate the direction of the muon drift by changing the collision frequency. The most straightforward way to modify the collision frequency is by changing the gas density. In the transverse compression stage, this is done by having the bottom of the apparatus at 6 K and the top at 19 K, thus creating a temperature gradient in the vertical ( $y$ -) direction. The gas pressure is chosen so that  $\frac{\nu_c}{\omega} = 1$  at  $y = 0$ . Muons at different  $y$ -positions (at fixed  $x$ -position) experience different densities, resulting in different drift directions: a muon stopped at the bottom of the target (higher density) experiences more collisions with He atoms ( $\frac{\nu_c}{\omega} > 1$ ) and will thus drift predominately in the  $\hat{E}$ -direction (large  $\theta$ , upwards), while a muon stopped in the top part (lower density) collides less frequently with He atoms ( $\frac{\nu_c}{\omega} < 1$ ), resulting in drift predominately in the  $\hat{E} \times \hat{B}$ -direction (small  $\theta$ , downwards). The net result is that muons

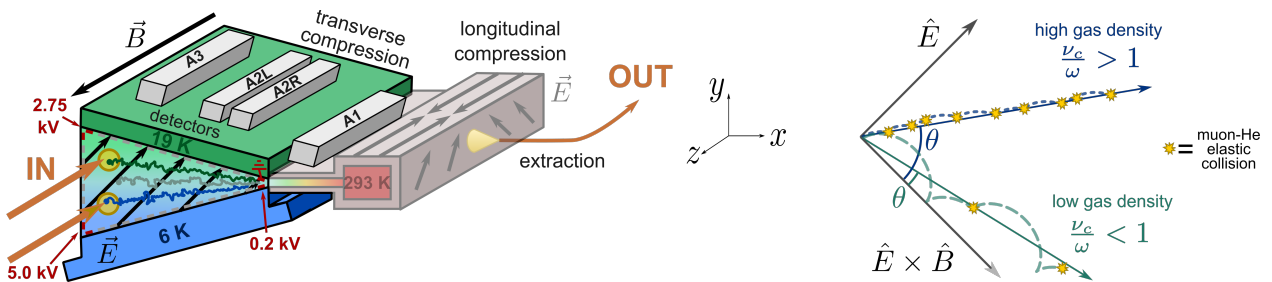


FIG. 1. (Left) Schematic diagram of the muCool device. A standard muon beam is stopped in a cryogenic helium gas target with a vertical temperature gradient inside a 5 T field. The extent of the stopped muons is reduced first in the transverse, then in the longitudinal direction. The sub-mm muon beam is extracted through an orifice into vacuum and re-accelerated along the  $z$ -axis. The electrodes used to define the required electric field in the transverse compression stage are also sketched (gray and red rectangles), along with the values of applied high voltage. (Right) Schematic of  $\mu^+$  trajectories in various gas densities and in crossed electric and magnetic fields.

stopped at different  $y$ -positions converge towards  $y = 0$ , while simultaneously drifting in the  $+x$ -direction. Hence, the muon beam spread is reduced in the  $y$ -direction to sub-mm size (transverse compression).

After that, the muons are transported to the second stage, which is at room temperature. In this stage, the electric field has a component parallel to the magnetic field and pointing towards  $z = 0$ , leading to a muon drift towards the center of the target, thus reducing muon spread in the  $z$ -direction (longitudinal compression). The vertical component of the electric field ( $E_y$ ) at this low density causes an additional drift in the  $\hat{E} \times \hat{B}$ -direction ( $+x$ -direction in this case), thus transporting the muons towards the final compression stage. From there, the sub-mm muon beam can be extracted through a small orifice into the vacuum, re-accelerated with pulsed electric fields to keV energies, and extracted out of the magnetic field (see Fig. 1). The efficient longitudinal compression of a muon beam, together with an  $\hat{E} \times \hat{B}$ -drift, has already been demonstrated [14, 15].

This Letter presents the first demonstration of the muon transverse compression stage of the muCool device. For this demonstration, about  $2 \cdot 10^4 \mu^+/s$  at 12.5 MeV/c were injected into the 25-cm-long target placed in the center of a 5-tesla solenoid. Before entering the target, the muons traversed a 55- $\mu\text{m}$ -thick entrance detector, several thin foils, and a copper aperture, defining the beam injection position.

The gas volume of the transverse target was enclosed by a Kapton foil, folded around triangular PVC end-caps. Kapton and PVC are both electrical and thermal insulators, and are thus capable of sustaining high voltage, while keeping the heat transport between top and bottom walls small. The large thermal conductivity of the single crystal sapphire plates glued to the top and the bottom target walls assured homogeneous temperatures of these walls. The required temperature gradient from 6 to 19 K was produced by heating the top wall with 500 mW power and thermally connecting the bottom wall

to a copper cold finger [16].

The Kapton foil enclosing the gas volume was lined with metallic electrodes extending along the  $z$ -direction. The 45° electric field was defined by applying appropriate voltages to several of these electrodes (see Fig. 1), which were connected to the rest of the electrodes via voltage dividers.

Several detectors were placed around the target, A1...A3 in Fig. 1, to monitor the muon movement by detecting the  $\mu^+$ -decay positrons. The detectors consisted of plastic scintillator bars with a groove inside which a wavelength-shifting fiber was glued. These 2 m-long wavelength-shifting fibers transported the scintillation light from the cryogenic temperatures in vacuum to room temperature and air, where they were read out by  $1.3 \times 1.3 \text{ mm}^2$  silicon photomultipliers. The scintillators were mounted inside a collimator to improve their position resolution.

The probability of detecting the decay positrons vs. the muon decay position is shown in Fig. 2 for the detectors A1 and A2L. By recording time spectra for each detector (with  $t = 0$  given by the muon entrance detector), we can observe indirectly the muon drift in the transverse target. To demonstrate transverse compression we also need to show that the muon beam size decreases during the drift. This is achieved by comparing the time spectra obtained when the temperature gradient (6–19 K at

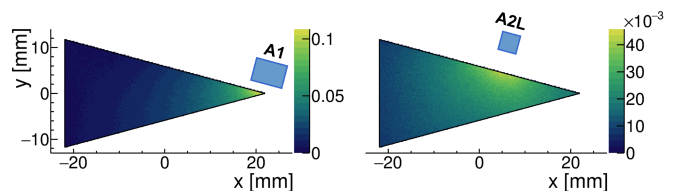


FIG. 2. Projection of the detection efficiency of the A1 and A2L positron detectors in the  $xy$ -plane, simulated with Geant4 [17]. The colorscale represents the positron detection efficiency.

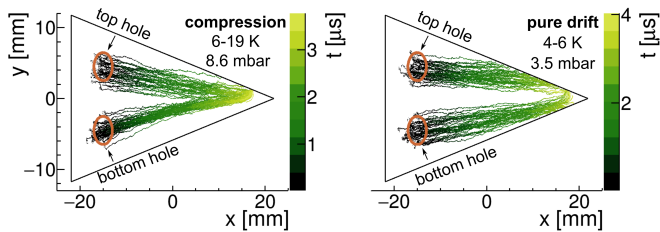


FIG. 3. Muon trajectories in the  $xy$ -plane simulated with Geant4 for the “top-hole” and “bottom-hole” injection and for the “compression” (left) and “pure-drift” (right) density conditions.

8.6 mbar) is applied, to the time spectra with negligible temperature gradient (4–6 K at 3.5 mbar): in the first case both drift and compression are expected; in the second only drift (“pure drift”). We further increased the contrast between “compression” and “pure-drift” measurements by injecting the muons through either “top hole” or “bottom hole” apertures at  $y = \pm 4.5$  mm (see Fig. 1). If we were to inject the muons through a single large aperture, the majority of the muons would be stopped close to  $y = 0$ , and would thus drift straight towards the tip for both “compression” and “pure drift.” Contrarily, with either of the two smaller apertures, we target only a narrow vertical region of the gas, with distinct density conditions for “compression” and “pure drift.”

Geant4 [17] simulations of the muon trajectories for “top-hole” and “bottom-hole” injections, and for “compression” and “pure drift,” are shown in Fig. 3, with an applied high voltage of  $HV = 5.0$  kV. The simulation included the most relevant low-energy  $\mu^+$  - He interactions: elastic collisions and charge exchange. The cross sections for these processes were appropriately scaled from the proton-He cross sections [12, 18]. Simulations show that for the “compression” case, muons injected through both apertures reach the tip of the target efficiently, while in the “pure drift” case, most of the muons stop in the target walls before reaching the tip.

The measured time spectra of A1 and A2L under “compression” conditions are presented in Fig. 4 (red dots), for both “top-” and “bottom-hole” injection. Note that the time spectra were corrected for muon decay by multiplying the counts by  $\exp(t/2.2 \mu\text{s})$ . The A1 counts increase with time, for both injection positions. This indicates that the muons were gradually moving towards the tip of the target, i. e., towards the A1 acceptance region (see Fig. 2). The A2L counts first increase, then decrease with time, suggesting that the muons first entered, then exited the acceptance region of the detector. After a certain time, the number of counts stays constant in both detectors, implying that the muons reached the target walls. For “bottom-hole” injection, the times at which muons reach the detector acceptance regions are delayed

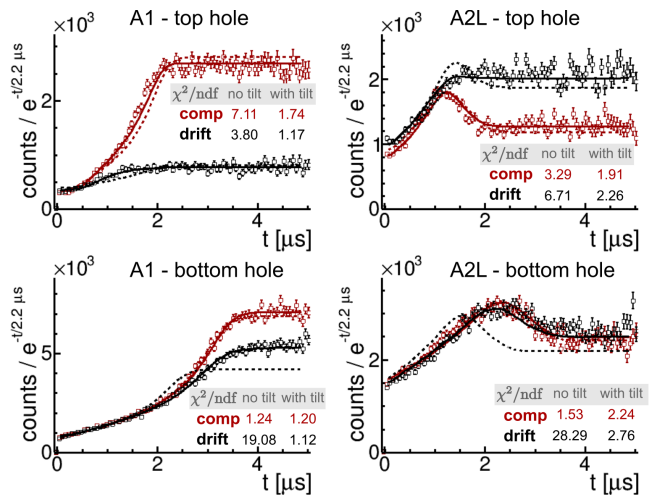


FIG. 4. Measured (points) A1 and A2L time spectra for “top-” and “bottom-hole” injection and for the “compression” (red) and “pure-drift” (black) conditions (see Fig. 3), along with corresponding simulated time spectra with (solid curves) and without (dashed curves) a small target misalignment. Each simulated time spectrum was fitted to the measured spectra using two fit parameters (normalization and flat background). The reduced chi-squared values of each fit are also indicated (ndf = 75).

by up to 1500 ns compared to the “top-hole” injection. Indeed, muons injected through the “bottom-hole” travel through a region of higher gas density compared to that for “top-hole” injection, leading to a slower drift. All these features are consistent with the simulation results of Fig. 3 (left).

The “pure-drift” time spectra for “top-hole” injection (black points in Fig. 4 (top row)) differ significantly from the “compression” time spectra. The A1 counts remain very low at all times, suggesting that the muons never reached the tip of the target. The A2L counts never decrease after reaching the maximum, implying that muons did not manage to “fly by” the detector, but they stopped in the target walls before leaving the acceptance region of the detector. This is consistent with the simulated trajectories of Fig. 3 (right). However, for “bottom-hole” injection, measured “pure-drift” time spectra (black points, Fig. 4 (bottom row)) are almost identical to the “compression” time spectra (red points). This is mainly due to detector resolution, which is worse for the “bottom-hole” measurements because muons drift at larger distances from the detectors.

To better compare the measurements with the Geant4 simulations, the muon trajectories of Fig. 3 were folded with the detector acceptance of Fig. 2 to produce the corresponding time spectra. These time spectra (dashed curves in Fig. 4) were then fitted to the measurements using two fit parameters per time spectrum: a normalization, to account for the uncertainties in the detection and stopping efficiencies, and a flat background, to ac-

count for beam-related stops in the walls. To improve the fits, the detector positions were shifted by up to 1 mm in the simulation compared to the design value, to account for possible shifts of various parts of the setup during the cool-down, and mechanical uncertainty. Relatively large reduced chi-squareds, especially for the “pure-drift” measurements, point to systematic discrepancies between the simulation and the measurements.

One possible explanation of the discrepancy could be a misalignment (tilt) between the target and the magnetic field axes. Even a small misalignment would shift the initial beam position, particularly affecting the “pure-drift” measurements, as the time and position at which muons crash into the target walls would shift accordingly. In the “compression” measurements, such misalignment is less problematic, because the temperature gradient ensures that muons reach the tip of the target, regardless of their initial position.

The effects of such misalignments were investigated by simulating time spectra for various tilts between the target and the magnetic field axes, and fitting them to the data. The best fit for “compression” and “pure drift” simultaneously was obtained by rotating the target axis from the (0, 0, 1) direction to (0.018, 0.007, 0.9998) for the “top hole,” and to (0.019, 0.005, 0.9998) for the “bottom hole,” leading to average shifts of the initial muon stopping distribution by up to 3.5 mm in the  $xy$ -plane.

Including such a tilt in the simulation improves the fit significantly (solid curves in Fig. 4). Even better agreement is achieved by allowing different tilts for the “compression” and “pure-drift” measurements, which likely points to a mismatch between the assumed and actual initial muon beam momentum distribution. Further possible improvements of the fit would be simultaneous fine-tuning of the tilt, the muon momentum distribution, and the detector positions. However, little further insight would be gained from such a time-consuming optimization, since the simulations presented here already reproduce well the main features of the measured time spectra. Hence, the measurements demonstrate the transverse compression of a muon beam.

Next, we investigate the muon drift versus its energy by varying the electric field strength. As explained above, the muon drift angle  $\theta$  is proportional to the average  $\mu^+$  - He collision frequency  $\nu_c$ , which can be written as

$$\nu_c = N\sigma_{MT}(E_{CM})|\vec{v}_r|, \quad (2)$$

where  $N$  is the helium number density,  $\sigma_{MT}(E_{CM})$  is the energy-dependent  $\mu^+$  - He momentum transfer cross section and  $\vec{v}_r$  is the  $\mu^+$  - He relative velocity.

For muon energies  $\lesssim 1$  eV,  $\sigma_{MT}$  is proportional to  $1/\sqrt{E_{CM}} \propto 1/|\vec{v}_r|$  [20], so that the collision frequency is independent of the muon energy. For energies larger than 1 eV, the product  $\sigma_{MT}|\vec{v}_r|$  decreases with energy, as shown in Fig. 5. Hence, the collision frequency and the muon drift angle  $\theta$  decrease with increasing muon energy.

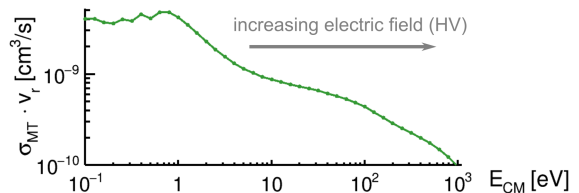


FIG. 5. Product  $\sigma_{MT} \cdot v_r$  vs. muon c.m. energy, using energy-scaled proton-He cross sections of [19].

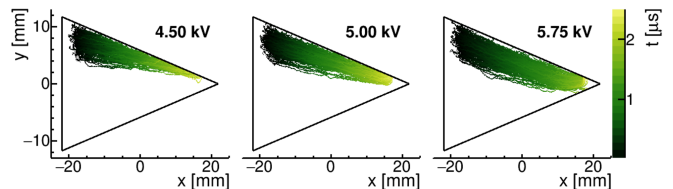


FIG. 6. Muon trajectories in the  $xy$ -plane for the “top hole” and “compression” conditions (6 – 19 K at 8.6 mbar), for various HV. The target axis was assumed to point in the (0.018, 0.007, 0.9998) direction, as determined previously by minimizing the chi-squared for the 5.0 kV measurements.

Since the muon energy in the He gas increases with electric field strength, the muon drift direction approaches the  $\vec{E} \times \vec{B}$ -direction with increasing electric field. The simulated muon trajectories of Fig. 6 for various applied HV confirm this behavior.

The dependence of the muon motion on the electric field strength was studied experimentally for various beam injections and density conditions. In Fig. 7 we present the measurements for “top-hole” and “compression” configuration, which illustrate all relevant features. We can see that the maximum number of counts in A1 decreases with decreasing HV, indicating that increasingly fewer muons reach the tip of the target. Moreover,

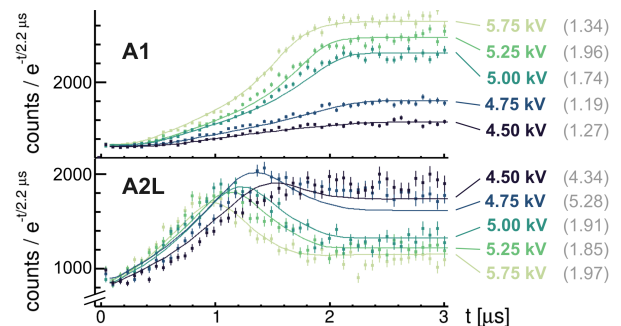


FIG. 7. Measured (points) A1 and A2L time spectra for “top-hole” and “compression” configuration and for various HV, scaled to have the same number of injected muons. Each simulated time spectrum (curves), corresponding to the trajectories of Fig. 6, was fitted to corresponding measured time spectrum using two free parameters (normalization and flat background). Chi-squared values are indicated in parentheses (ndf = 75).

for smaller HV the drift is slower, as visible from the shift of the A2L time spectrum maximum towards later times. This is consistent with the simulated trajectories of Fig. 6.

The simulated time spectra for each HV and for each detector were fitted independently to the measurements with two free parameters: normalization and flat background. It was not possible to perform a simultaneous fit for all HV values. We indeed observed that the normalization giving the best fit depends systematically on the HV. This might be caused by the lack of a precise definition of the electric field at the target tip, which would affect most significantly the measurements with strong electric fields, where muons actually reach the tip of the target. A mismatch of the initial muon stop distribution between simulations and experiment would also contribute to this systematic effect.

Still, the simulation reproduces correctly the muon drift velocity, which is given by the energy-dependent  $\mu^+$  - He elastic cross section. Indeed, the maxima of the time spectra, occurring when muons arrive in the detector acceptance region, are consistent between measurements and simulations.

To summarize, this Letter presents the first demonstration of transverse compression of a muon beam with the muCool device. One critical aspect of this demonstration was distinguishing between a simple muon drift versus drift with simultaneous reduction of the beam transverse size. Such distinction was accomplished by performing the measurements with and without a vertical temperature gradient, which is needed for the transverse compression, and by injecting the muon beam into different density regions of the target. The muon motion corresponding to realistic experimental conditions was simulated using the Geant4 package including custom low-energy ( $< 1$  keV) muon processes [18]. Very good agreement between the simulations and measurements was achieved after accounting for small target and detector misalignments. According to the simulations, under these experimental conditions, a muon beam with initial diameter of 10 mm and 830 keV energy with 17 keV spread is transformed within 3.5  $\mu$ s into a beam of 0.7 mm size (FWHM) in the  $y$ -direction and 5 eV energy with 5 eV spread.

Besides demonstrating the transverse compression, the dependence of the muon drift on the applied electric field strength was explored experimentally and found to be in fair agreement with Geant4 simulations. This validates our modeling of the low-energy  $\mu^+$  - He elastic collisions.

Connecting the transverse compression stage demonstrated in this Letter to the previously demonstrated longitudinal compression stage [14, 15] will allow us to realize a high-brightness low-energy muon beam as proposed in [12], with a phase space compression factor of  $10^{10}$  and  $10^{-3}$  efficiency relative to the input beam.

The experimental work was performed at the  $\pi E1$

beamline at the PSI proton accelerator HIPA. We thank the machine and beam line groups for providing excellent conditions. We gratefully acknowledge the outstanding support received from the workshops and support groups at ETH Zurich and PSI. Furthermore, we thank F. Kottmann, M. Horisberger, U. Greuter, R. Scheuermann, T. Prokscha, D. Reggiani, K. Deiters, T. Rauber, and F. Barchetti for their help. This work was supported by the SNF grants No. 200020\_159754 and 200020\_172639.

---

\* aldo@phys.ethz.ch

† ivanabe@phys.ethz.ch

‡ *Present address:* Tsung-Dao Lee Institute, and School of Physics and Astronomy, Shanghai Jiao Tong University, Shanghai 200240, China

§ *Present address:* Laboratory for High Energy Physics, Albert Einstein Center for Fundamental Physics, University of Bern, CH-3012 Bern, Switzerland

¶ *Present address:* Laboratory of Physical Chemistry, ETH Zürich, 8093 Zürich, Switzerland

- [1] T. Gorringer and D. Hertzog, *Prog. Part. Nucl. Phys.* **84**, 73 (2015).
- [2] H. Inuma, *J. Phys. Conf. Ser.* **295**, 012032 (2011).
- [3] A. Adelman, K. Kirch, C. J. G. Onderwater, and T. Schietinger, *J. Phys. G Nucl. Part. Phys.* **37**, 085001 (2010).
- [4] A. Crivellin, M. Hoferichter, and P. Schmidt-Wellenburg, *Phys. Rev. D* **98**, 113002 (2018).
- [5] P. Crivelli, *Hyperfine Interact.* **239**, 49 (2018).
- [6] K. Kirch and K. S. Khaw, *Int. J. Mod. Phys. Conf. Ser.* **30**, 1460258 (2014), arXiv:1509.02918.
- [7] A. Antognini *et al.*, *Atoms* **6**, 17 (2018).
- [8] S. van der Meer, *Rev. Mod. Phys.* **57**, 689 (1985).
- [9] G. I. Budker and A. N. Skrinski, *Sov. Phys. Uspekhi* **21**, 277 (1978).
- [10] M. Mühlbauer, H. Daniel, *et al.*, *Hyperfine Interact.* **119**, 305 (1999).
- [11] E. Morenzoni, F. Kottmann, *et al.*, *Phys. Rev. Lett.* **72**, 2793 (1994).
- [12] D. Taquq, *Phys. Rev. Lett.* **97**, 10 (2006).
- [13] A. E. D. Heylen, *IEE Proc. A (Physical Sci. Meas. Instrumentation, Manag. Educ. Rev.)* **127**, 221 (1980).
- [14] Y. Bao, A. Antognini, *et al.*, *Phys. Rev. Lett.* **112**, 224801 (2014).
- [15] I. Belosevic, A. Antognini, *et al.*, *Eur. Phys. J. C* **79**, 430 (2019).
- [16] G. Wichmann, A. Antognini, *et al.*, *Nucl. Instruments Methods Phys. Res. Sect. A Accel. Spectrometers, Detect. Assoc. Equip.* **814**, 33 (2016).
- [17] S. Agostinelli *et al.*, *Nucl. Instruments Methods Phys. Res. Sect. A Accel. Spectrometers, Detect. Assoc. Equip.* **506**, 250 (2003).
- [18] I. Belosevic, *Simulation and experimental verification of transverse and longitudinal compression of positive muon beams: Towards a novel high-brightness low-energy muon beam-line*, Ph.D. thesis, ETH Zurich (2019).
- [19] D. R. Schultz and P. S. Krstic, *At. Energy* **8** (1998).
- [20] E. A. Mason, S. L. Lin, and I. R. Gatland, *J. Phys. B At. Mol. Phys.* **12**, 4179 (1979).